Quantitative Measurement of Temperature-Dependent Quasiparticle Scattering of the Topological Surface States in Bi_2Se_3

Shengyue Lu[1,2], Yeqinbo Zhang[1], Xueyan Ma[1], Jingze Li[1], Yongkai Deng[1], and Yunquan Liu[1,2,3,4*]

[1]*State Key Laboratory for Mesoscopic Physics and Collaborative Innovation Center of Quantum Matter, School of Physics, Peking University, Beijing 100871, China*
[2]*Beijing Academy of Quantum Information Sciences, Beijing 100193, China*
[3]*Collaborative Innovation Center of Quantum Matter, Beijing 100871, China*
[4]*Peking University Yangtze Delta Institute of Optoelectronics, Nantong 226010, China*

(Received 1 November 2024; accepted manuscript online 24 December 2024)

The quasiparticle scattering processes of the topological surface state (TSS) in three-dimensional topological insulators (TIs) have a vital effect on the many-body interactions and potential applications of topological materials. In this study, we performed high-resolution temperature-dependent angle-resolved photoemission spectroscopy analysis of the 3D strong TI Bi_2Se_3. Using an *ab initio* simulation, we analyzed the temperature dependence of the electronic structure and lifetime broadening of the TSS, which are closely associated with the quasiparticle scattering process, i.e., electron–phonon coupling and spin-dependent scattering. We show that, at a low temperature (7 K), the spin-dependent electron scattering facilitates the anisotropic scattering rate of the TSS. Conversely, at room temperature (300 K), the electron–phonon coupling dominates the contribution to the scattering rate. The scattering rate increases with temperature and becomes uniform in momentum space owing to the temperature dependence of quasiparticle scattering. The quantitative study of temperature-dependent scattering rates in TSS is crucial to understanding the topological property and transport mobility of Dirac fermions for fundamental studies and potential applications.

DOI: 10.1088/0256-307X/42/1/017303 CSTR: 32039.14.0256-307X.42.1.017303

The three-dimensional topological insulator (TI), a newly discovered quantum matter, has an insulating bulk state and a gap-closing surface state.[1–3] Electrons in the surface state exhibit a linear dispersion relation and a spin-momentum locking texture, compatible with massless Dirac fermions. Time-reversal symmetry guarantees the robustness of the topological surface state (TSS) against time-reversal-invariant perturbations, such as nonmagnetic impurities and crystalline defects. Because of their intriguing topological nature, TIs have wide applications in spintronics[4,5] and quantum computing[5,6] and serve as promising platforms for studying novel physical phenomena such as Majorana fermions,[7] magnetic monopoles,[8] and the quantum spin Hall effect.[9]

Although backscattering would be forbidden, other scattering processes of electrons occur in the TSS, such as electron–electron interaction, electron–phonon coupling, and electron–disorder interaction in the surface state,[10–12] which largely determine the lifetime of the quasiparticles and the electron mobility in the transport process.[13] Understanding and controlling this many-body interaction in condensed matter physics is fundamental as it plays a significant role in the band renormalization,[14] the formation of electron pairs (Cooper pairs),[15] and the robustness of the TSS.[16] The influence and manipulation on the scattering process of the TSS has been widely studied using different techniques, including scanning tunneling microscopy (STM),[17,18] Raman spectroscopy,[19] and in particular, angle-resolved photoemission spectroscopy (ARPES).[20] For example, electron–phonon coupling has been discussed in theory[21,22] and measured at different temperatures in high-resolution ARPES measurements.[23–25] The electronic interference based on the spin-dependent scattering in the strongly warped Dirac cone has also been studied using experiments.[26,27] The electron–phonon coupling in the TI system is essential in the excited carrier bulk-surface transfer and depends significantly on the temperature.[28] Recently, theoretical studies have shown that the temperature dependence of relaxation dynamics in Bi_2Te_3 is governed by electron–phonon and spin–phonon coupling.[29] However, the qualitative temperature dependence of the quasiparticle scattering in 3D TIs has not been experimentally studied.

Herein, we present a high-resolution time-of-flight (TOF)-ARPES study on the electronic structure of Bi_2Se_3. The temperature-dependent dispersion relation of the surface state was studied. As the temperature increases, the Dirac cone is compressed, and the conduction band bottom moves downward. This temperature-dependent band change was confirmed using an *ab initio* simulation based on the electron–phonon coupling. Additionally, we analyzed the quasiparticle scattering of the surface state

*Corresponding author. Email: Yunquan.liu@pku.edu.cn
© 2025 Chinese Physical Society and IOP Publishing Ltd. All rights, including for text and data mining, AI training, and similar technologies, are reserved.

and experimentally observed the anisotropy of the lifetime broadening of the TSS at low temperatures. This anisotropic behavior can be explained by spin-dependent scattering. In the experiment, we observed the transition of the dominant scattering mechanism at different temperatures, which was manifested in the lack of sixfold symmetry on the scattering rate as the temperature increased. This phenomenon is caused by the enhancement of the electron–phonon and inter-band scattering and reveals the temperature dependence of quasiparticle scattering.

We performed temperature-dependent ARPES measurements on Bi_2Se_3. The experimental details are given in the Supplemental Material. Figure 1(a) shows the measured Fermi surface of the band structure captured at $E = E_F$ at 7 K. This constant energy contour concludes the inner bulk state and outer surface state with a hexagon-shaped contour. Owing to the photoelectron escape depth, the bulk conduction band is weak compared with the TSS. The measured hexagonally warped Fermi surface results from cubic spin–orbit coupling and affects the spin texture of the Dirac cone,[30,31] which is the basis for the subsequent analysis. The spin directions of electrons on the Fermi surface, involving unpolarized bulk states (dashed lines) and polarized TSS, have been verified in other spin-resolved ARPES studies.[32,33] Figure 1(b) depicts the cut of the electronic structure captured along the momentum direction ($k_x = 0$). The Dirac cone surface states can be observed clearly. The measured sample Bi_2Se_3 was electron-doped (n-type); therefore, the Fermi level was above the bulk valence band, located at about 400 meV above the Dirac point. The Fermi velocity of the electron was estimated to be approximately 4×10^5 m/s.

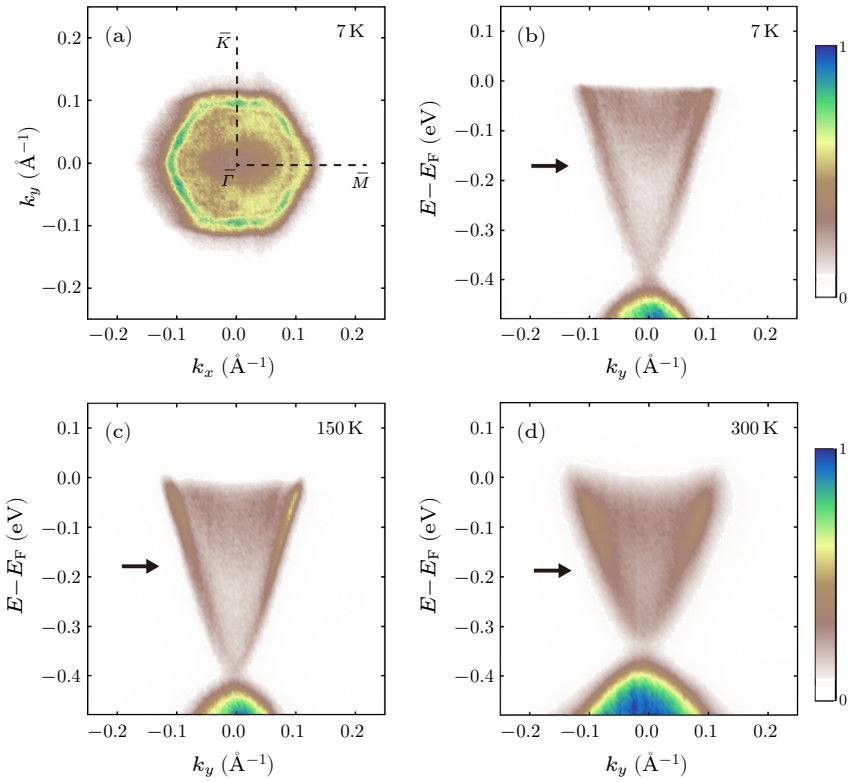

Fig. 1. ARPES data of Bi_2Se_3. (a) Fermi surface of Bi_2Se_3 at 7 K. (b)–(d) Surface state dispersion along the $\overline{\Gamma K}$ direction at different temperatures. The arrows indicate the bottom of the conduction band.

Within the Koopmans' photoexcitation theorem,[34] an $(N-1)$-electron system can be affected by many-body interactions in terms of scattering and band renormalization.[34] Generally, three scattering channels are considered to contribute linearly to the total scattering rate Γ,[36] including electron–electron scattering Γ_{e-e}, electron–phonon scattering Γ_{e-ph}, and electron impurity scattering Γ_{imp},[13,37]

$$\Gamma = \Gamma_{e-e} + \Gamma_{e-ph} + \Gamma_{imp}. \quad (1)$$

Electron impurity scattering primarily depends on the doping concentration and environment. Electron–electron scattering depends on the shape of the Fermi surface, and its temperature-dependent contribution has been shown to be nearly negligible.[36] For electron–phonon scattering, within the energy $|\omega| < \omega_{max}$, where ω_{max} is the highest energy of the involved phonons, higher temperature activates more phonon modes and significantly strengthen the electron–phonon scattering. To reveal the characteristics of different scattering mechanisms in the TSS, we measured the temperature-dependent ARPES of Bi_2Se_3.

The surface state bands along the direction of $\overline{\Gamma K}$ in the temperature-dependent ARPES measurements are shown in Figs. 1(b)–1(d) at 7, 150, and 300 K, respectively. During the time of data collection, the TSS was very stable under a constant temperature, without any noticeable changes in electronic structure in several hours. Therefore, the phenomenon shown in Figs. 1(b)–1(d) reflects

the intrinsic changes of quasiparticle dynamics induced by temperature, rather than the disturbance caused by the adsorption or desorption of residual gases at different temperatures.[38] This is also briefly discussed in the Supplemental Material. Despite the temperature-dependent modification of the surface state, we could not detect any gap opening at the Dirac point, and the Dirac cone could still be observed even at room temperature. This phenomenon confirms that the TSS is robust against bulk band modification derived from the electron–phonon interaction at finite temperatures, consistent with topological protection.[1] As the temperature increases, more electrons are transferred to states above the Fermi level, and the TSS is broadened. The temperature broadening of the TSS reflects an increase in the scattering on phonons and the electron–phonon coupling constant.[23] Additionally, we could also clearly observe the shift of the Dirac point is approximately 80 meV from 7 to 300 K.

To further investigate the band modification induced by temperature in Bi_2Se_3, we obtained the momentum-integrated energy distribution curves (EDCs) as a function of sample temperature, as shown in Fig. 2(a). The energy distribution around the Fermi level became vague with increasing temperature. This resulted from the thermal excitation to energy levels above the chemical potential according to the temperature-dependent Fermi–Dirac distribution. The Dirac point is highlighted by red crosses, and its binding energy exhibited a gradual upward trend, particularly above 100 K, as shown in Fig. 2(a). We also extracted the momentum distribution curves (MDCs) at the Fermi energy measured at different temperatures along the direction of $\overline{\Gamma K}$, as shown in Fig. 2(b). As the temperature increased, the magnitude of the wave vectors at E_F (Fermi wave vector, k_F) remained almost constant, and the peaks at k_F in the MDCs broadened slightly. This broadening reflected the increase in the lifetime of quasiparticles and enhancement of electron–phonon scattering with the increase in temperature.[24,39]

The EDCs extracted from the surface state and bulk state at different temperatures are shown in Figs. 2(c) and 2(d), respectively. The surface states were accurately identified by fitting the data with a Lorentzian lineshape to obtain the peaks. The EDC of the bulk state was extracted by integrating the electron distribution within the Dirac cone after removing the contribution from the surface states. The arrows represent the Dirac point in Fig. 2(c) and the conduction band bottom in Fig. 2(d). With the increase in temperature, the Dirac point shifted upwards, and the Dirac cone was compressed along the energy direction, as shown in Fig. 2(c). For the bulk state, the density of states near the Fermi edge increased at room temperature, as shown in Fig. 2(d). Additionally, the decrease in the energy of the conduction band bottom indicated the downward shift of the conduction band. Consequently, a broader overlap was observed between the bulk conduction band and TSS in the energy distribution, which promoted the bulk–surface scattering by increasing the available phase-space volume.[13]

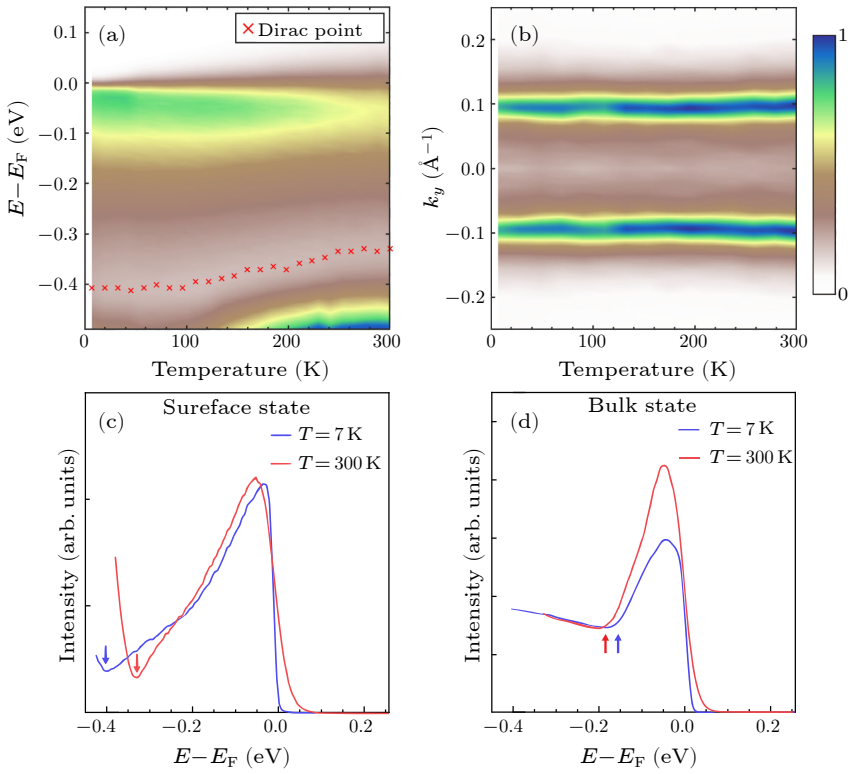

Fig. 2. (a) EDCs and (b) MDCs of Bi_2Se_3 measured at the temperature ranging from 7 to 300 K. (c) EDCs of the surface state measured at 7 and 300 K. The arrows indicate the Dirac point. (d) EDCs above the Dirac point extracted from the bulk state at 7 and 300 K. The arrows indicate the bottom of the conduction band.

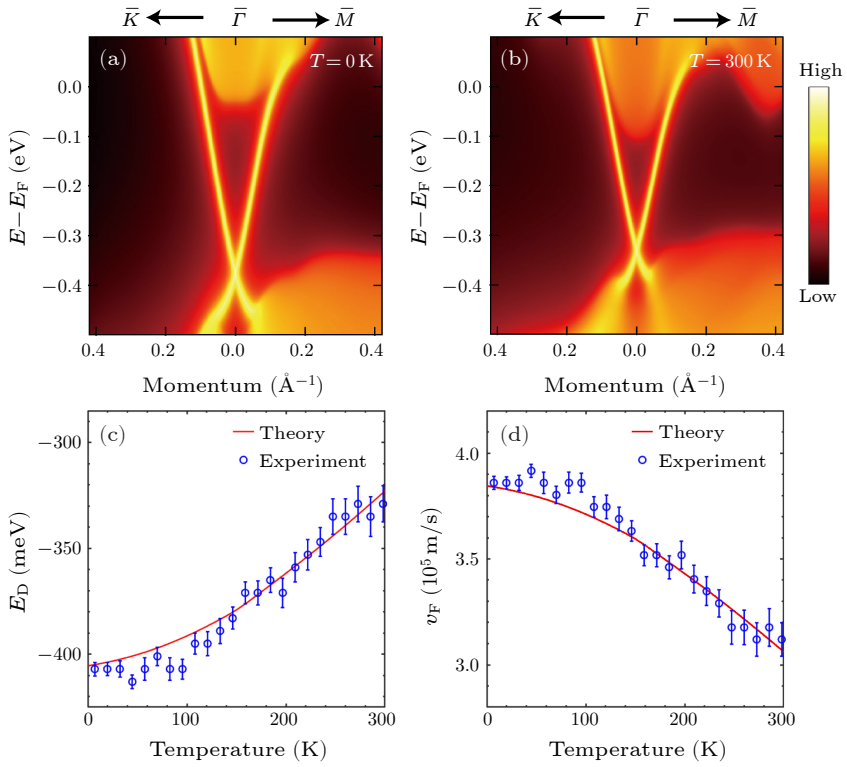

Fig. 3. Calculated topological surface state in $T = 0$ K (a) and $T = 300$ K (b). Temperature dependence of the binding energy of the Dirac point and Fermi velocity in the experiment (blue mark) and in theory (red line).

To study temperature-dependent band modification, we calculated the electronic structure at different temperatures. The details of the calculation are shown in the Supplemental Material. The electronic structures of Bi_2Se_3 calculated at $T = 0$ K and $T = 300$ K are shown in Figs. 3(a) and 3(b). We can clearly observe a single Dirac cone at the Γ point and distinguish the contribution from the bulk and surface states at different temperatures. Additionally, the energy for the conduction band bottom at the Γ point decreased at high temperatures, and more electrons in the bulk state were distributed above the Dirac point, caused by phonon-induced deviation from atomic equilibrium sites.[40] We also extracted and compared the binding energy of Dirac point and Fermi velocity from ARPES data (blue markers) and simulation (red lines), which are shown in Figs. 3(c) and 3(d) respectively. As the temperature increased from 0 to 300 K, the upward shift of the Dirac point was approximately 70 meV in our simulation, as observed in Fig. 3(c). The temperature dependence of the Dirac point and the Fermi velocity in the experiment and calculation agreed closely. Our results revealed that the modification for bulk state and TSS approached each other in the energy distribution induced by electron–phonon scattering. This phenomenon results in a higher probability of bulk state interacting with the TSS at room temperature.[24,39]

To study the scattering process more thoroughly, we performed a detailed self-energy analysis of the TSS spectral data extracted from the ARPES. Under the sudden approximation, various complicated effects induced by the many-body interaction in solids can be included in a single function called self-energy $\Sigma(\boldsymbol{k}, \omega)$.[35] $\Sigma(\boldsymbol{k}, \omega)$ can be extracted from the single-particle spectral function $A(\boldsymbol{k}, \omega)$ given by

$$A(\boldsymbol{k}, \omega) = \frac{1}{\pi} \frac{|\operatorname{Im}\Sigma(\boldsymbol{k}, \omega)|}{[\omega - \epsilon_{\boldsymbol{k}} - \operatorname{Re}\Sigma(\boldsymbol{k}, \omega)]^2 + [\operatorname{Im}\Sigma(\boldsymbol{k}, \omega)]^2}. \quad (2)$$

Here, $\boldsymbol{k}$ and ω represent the electron momentum and energy, respectively. The real part of the self-energy $\operatorname{Re}\Sigma$ is the energy difference between the renormalized and bare bands. The imaginary part of the self-energy $\operatorname{Im}\Sigma$ is extracted from the width of the Lorentzian peaks in MDCs, which reflects the scattering rate and lifetime of the quasiparticles. The scattering rates of electrons can be expressed as $\Gamma = 2\operatorname{Im}\Sigma$.[41]

The real and imaginary parts of the self-energy versus energy along the $\overline{\Gamma K}$ and $\overline{\Gamma M}$ at 7 K are shown in Figs. 4(a) and 4(b), respectively. The electron–phonon scattering was characterized by the peak in $\operatorname{Re}\Sigma$ at approximately 20 meV, consistent with the highest-frequency phonon mode (A_{1g}^2), as shown in Fig. S1 in the Supplemental Material. The slope of $\operatorname{Re}\Sigma$ of the electron near the E_F determines the electron–phonon scattering strength.[37] For $\operatorname{Im}\Sigma$, it exhibited significant differences on the Fermi surface, which was higher along the $\overline{\Gamma K}$ direction.

For a more intuitive comparison, we expressed photoelectron counts as a function of Δk (the deviation from k_F) measured at 7 K along $\overline{\Gamma M}$ and $\overline{\Gamma K}$ direction, as shown in Fig. 4(c). The width of the peaks was larger along the $\overline{\Gamma K}$ direction, representing a longer quasiparticle lifetime. Furthermore, we analyzed MDCs along different directions in momentum space and calculated their scattering rates (blue marks) through self-energy analysis, as shown in Fig. 4(d). The scattering rates along different

directions exhibited significant disparities, with the highest along $\overline{\Gamma K}$ and the lowest along $\overline{\Gamma M}$. The anisotropic behavior of the scattering rates exhibited hexagonal symmetry, similar to the structure of the hexagonally deformed Fermi surface of Bi_2Se_3. To eliminate the contribution of the dipole matrix elements modulating the photoemission process, we also applied s-polarized pulses to probe the sample. The anisotropy of the scattering rates remained regardless of the polarization of the excited light. This suggested that our observation was related to the electronic structure of the TSS in the ground state rather than light-induced changes.

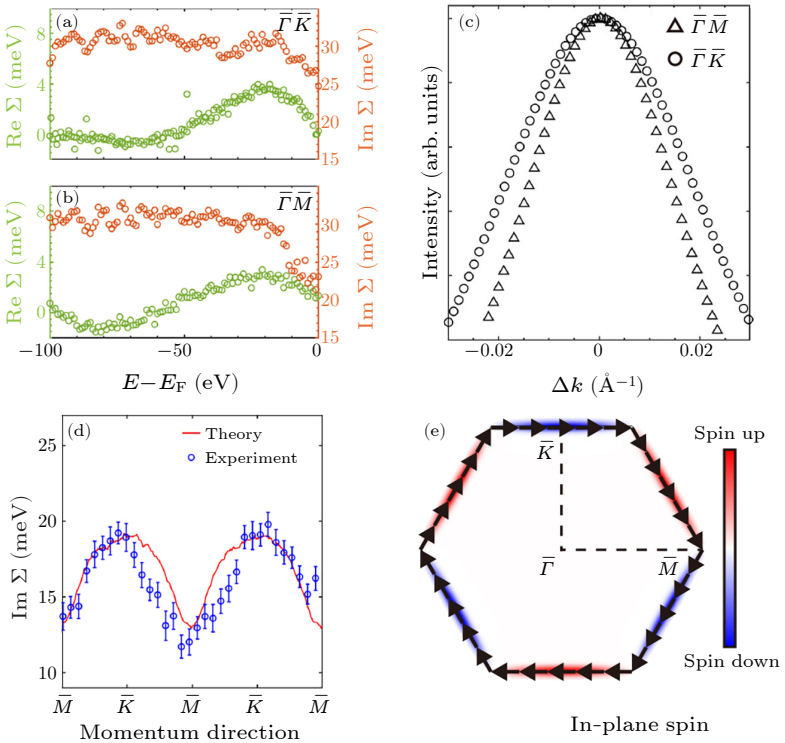

Fig. 4. Self-energy analysis along the $\overline{\Gamma K}$ (a) and $\overline{\Gamma M}$ (b) at 7 K. (c) MDCs along the $\overline{\Gamma M}$ and $\overline{\Gamma K}$ as a function of Δk ($\Delta k = k - k_F$). (d) Spin-dependent scattering rate along different directions in k space in the experiment (blue mark) and in theory (red line). (e) Schematics of the spin direction of the TSS in Bi_2Se_3. The black arrows indicate the in-plane spin direction.

The anisotropic behavior of the scattering rates in TSS is associated with the spin-dependent scattering (SPS) in the warping Fermi surface.[26] Although the backscattering is forbidden in the chiral spin texture, the scattering away from 180° is not completely suppressed.[42] The elastic scattering probability between the initial and final states on the same constant-energy contour can be expressed as[18]

$$P(\boldsymbol{q}) = \int_{\boldsymbol{k}} I(\boldsymbol{k}) T(\boldsymbol{q}, \boldsymbol{k}) I(\boldsymbol{k}+\boldsymbol{q}) d\boldsymbol{k}, \tag{3}$$

where $I(\boldsymbol{k})$ is the spectral weight, corresponding to the ARPES-measured density of states. $T(\boldsymbol{q}, \boldsymbol{k})$ is the scattering matrix element ($\hbar\boldsymbol{q}$ is the momentum transfer), which is related to the overlapping between the spin configuration of the initial and final states involved in the scattering event. As a result, the scattering probability is affected by the electron spin texture. Taking the Fermi surface of the TSS in Bi_2Se_3 as an example, as shown in Fig. 4(e), the constant-energy contour is deformed to the hexagonal shape by cubic spin–orbit coupling.[30,31] The in-plane spin direction is tangential to the constant energy contour and the out-plane spin direction is modulated with maximally upward (red) and downward (blue) along the $\overline{\Gamma K}$ direction. With respect to the in-plane component, the spin directions change more intensely in the vicinity of the $\overline{\Gamma M}$ direction, whereas the spin directions in the vicinity of the $\overline{\Gamma K}$ direction are fully parallel to each other, resulting in stronger contribution to the scattering probability. For the out-plane spin direction, scattering event near the $\overline{\Gamma M}$ direction, where $s_z = 0$, has a slight overlap between the initial and final states. Therefore, the scattering rate along the $\overline{\Gamma K}$ direction is enhanced, which is absent in an ideally circular Dirac cone.

To achieve more intuitive understanding about the anisotropic scattering within TSS, we consider the spin-dependent scattering matrix element of the form $T(\boldsymbol{q}, \boldsymbol{k}) = |\langle \boldsymbol{s}(\boldsymbol{k}) \mid \boldsymbol{s}(\boldsymbol{k}+\boldsymbol{q})\rangle|^2$ to evaluate the scattering rate in TSS quantitatively, which represents the scattering amplitude between two different spin states $\boldsymbol{s}(\boldsymbol{k})$ and $\boldsymbol{s}(\boldsymbol{k}+\boldsymbol{q})$.[18,42] This matrix element primarily depends on the momentum transfer. The contribution to the total scattering at certain $\boldsymbol{k}$ values can be calculated using the sum of individual matrix elements for all possible $\boldsymbol{q}$ vectors. In this model, the scattering between states with aligned spins is enhanced,

and the scattering between states with opposite spin orientations is eliminated. The calculated scattering rate as a function of momentum direction (red line) is shown in Fig. 4(d). We observe that the calculated scattering rate varies significantly with the direction of momentum, being maximum along the $\overline{\Gamma K}$ direction and minimum along the $\overline{\Gamma M}$ direction, which corresponds with the experiment (blue marks). The calculated results quantitatively illustrate the anisotropic scattering behavior induced by spin-dependent scattering.

Next, we will further analyze the temperature dependence of the scattering process. In theory, the interplay between different scattering events is difficult. Here, we can estimate their strength individually, if we consider their independent contribution to the total scattering rate. Based on the assumption that electrons and phonons are in a thermal quasi-equilibrium, the collision integral and relaxation time for electron–electron and electron–phonon interactions can be estimated using analytic expressions as descriptors of the interaction strength.[43–46] We calculated the scattering strength with respect to the temperature including the electron–phonon and spin-dependent electron–electron interactions on the Fermi surface, as shown in Fig. 5(a). The scattering strength varies with momentum at low temperatures, whereas this dependence vanishes as the temperature increases. In the experiments, we also analyzed the scattering behavior at different temperatures. The cross-section of the scattering rate of the TSS of the surface Brillouin zone measured at 7, 150, and 300 K is shown in Fig. 5(b). As the temperature increased, the scattering process became stronger and the cross-section exhibited the lack of sixfold symmetry. The experimental observation was recaptured by the theoretical calculation. The observed profiles at 150 and 300 K appeared as elongated ellipses along the 30-degree direction, which was attributed to inherent material inhomogeneities and defects.

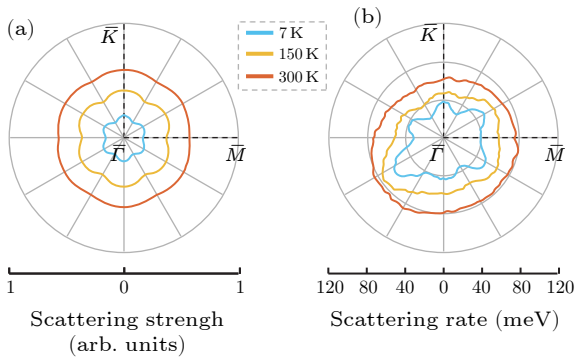

Fig. 5. (a) Calculated scattering strength of TSS with different momentum including the electron–electron and electron–phonon interactions at different temperatures in our calculation. (b) Measured scattering rate along different directions in k space experimentally at 7, 150, and 300 K.

This phenomenon is related to the temperature dependence of the scattering process, which can be illustrated within three aspects. (i) For the electron–phonon scattering, $\Gamma_{\mathrm{e-ph}}$ is approximately proportional to the temperature as explained with the Eliashberg function.[23] The increment in $\mathrm{Im}\,\Sigma$ is larger than 25 meV after heating to room temperature. The electron–phonon scattering is nearly isotropic, as observed in the evidence in the self-analysis of ARPES measurement.[37] (ii) For the electron–electron scattering, the temperature-dependent contribution of $\Gamma_{\mathrm{e-e}}$ is negligible, being of the order of 0.1 meV at room temperature.[36] The anisotropy of the spin-dependent scattering is determined by the intrinsic spin texture of the TSS, which remains stable at room temperatures.[47] (iii) The inter-band scattering between the TSS and unpolarized bulk state is not spin-selective and also contributes to the temperature dependence of quasiparticle scattering. The temperature-induced band change shown in Fig. 2 and Fig. 3 indicates that the bulk-surface scattering is enhanced at room temperature. Consequently, increasing temperature will weaken the intrinsic anisotropic scattering. More phonon modes interact with quasiparticles as the temperature increasing, and the isotropic increment of scattering rate induced by the electron–phonon scattering and inter-band scattering will dominate over the inherent anisotropic behavior induced by spin-dependent scattering.

In summary, we studied the temperature-dependent electronic structure and quasiparticle scattering of the TSS in 3D strong TI Bi_2Se_3. We analyzed the electronic structure of TSS at different temperatures based on an ARPES experiment and first-principles calculation. The study reveals the temperature dependence of electronic structure. The Dirac cone is compressed and the conduction band bottom moves downward. Through calculating the self-energy as well as the spin-dependent scattering matrix element, we explain the anisotropy of the lifetime broadening of the TSS in Bi_2Se_3 at low temperature (7 K). Additionally, we show the scattering process in TSS changes from six-fold symmetric anisotropy to a more uniform distribution as the temperature increased, as a result of the enhancement of the electron–phonon scattering and inter-band scattering. Our study demonstrates the temperature dependence of quasiparticle scattering and the transition of the dominant scattering process concerning temperature. The quantitative study of the temperature-dependent band change and the effect of the scattering process is very crucial as it provides a new perspective on the topological property and transport mobility with respect to the temperature.

Acknowledgments. This work was supported by the National Key R&D Program of China (Grant No. 2022YFA1604301) and the Natural Science Foundation of China (Grant Nos. 12334013, 12204018, 92050201, and 92250306).

References

[1] Hasan M Z and Kane C L 2010 *Rev. Mod. Phys.* **82** 3045
[2] Moore J E 2010 *Nature* **464** 194
[3] Qi X L and Zhang S C 2011 *Rev. Mod. Phys.* **83** 1057
[4] He Q L, Hughes T L, Armitage N P, Tokura Y, and Wang K L 2022 *Nature Mater.* **21** 15
[5] He M, Sun H, and He Q L 2019 *Front. Phys.* **14** 43401

[6] Koh J M, Tai T, and Lee C H 2022 *Phys. Rev. Lett.* **129** 140502
[7] Fu L and Kane C L 2008 *Phys. Rev. Lett.* **100** 096407
[8] Qi X L, Li R, Zang J, and Zhang S C 2009 *Science* **323** 1184
[9] Bernevig B A, Hughes T L, and Zhang S C 2006 *Science* **314** 1757
[10] Toporov Yu V and Kordyuk A A 2019 *Low Temp. Phys.* **45** 118
[11] LaShell S, Jensen E, and Balasubramanian T 2000 *Phys. Rev. B* **61** 2371
[12] Sánchez-Barriga J, Battiato M, Krivenkov M *et al.* 2017 *Phys. Rev. B* **95** 125405
[13] Park S R, Jung W S, Kim C *et al.* 2010 *Phys. Rev. B* **81** 041405
[14] Garate I 2013 *Phys. Rev. Lett.* **110** 046402
[15] Chen A Q, Park M J, Gill S T *et al.* 2018 *Nat. Commun.* **9** 3478
[16] Kim S, Yoshizawa S, Ishida Y *et al.* 2014 *Phys. Rev. Lett.* **112** 136802
[17] Zhang T, Cheng P, Chen X *et al.* 2009 *Phys. Rev. Lett.* **103** 266803
[18] Okada Y, Dhital C, Zhou W *et al.* 2011 *Phys. Rev. Lett.* **106** 206805
[19] Buchenau S, Scheitz S, Sethi A *et al.* 2020 *Phys. Rev. B* **101** 245431
[20] Wang Y H, Hsieh D, Sie E J *et al.* 2012 *Phys. Rev. Lett.* **109** 127401
[21] Giraud S and Egger R 2011 *Phys. Rev. B* **83** 245322
[22] Zhu X T, Santos L, Sankar R *et al.* 2011 *Phys. Rev. Lett.* **107** 186102
[23] Hatch R C, Bianchi M, Guan D *et al.* 2011 *Phys. Rev. B* **83** 241303
[24] Pan Z H, Fedorov A V, Gardner D *et al.* 2012 *Phys. Rev. Lett.* **108** 187001
[25] Kumar A, Kumar S, Miyai Y, and Shimada K 2022 *Phys. Rev. B* **106** L121104
[26] Sánchez-Barriga J, Scholz M R, Golias E *et al.* 2014 *Phys. Rev. B* **90** 195413
[27] Kim S, Ye M, Kuroda K *et al.* 2011 *Phys. Rev. Lett.* **107** 056803
[28] Kim D, Li Q, Syers P *et al.* 2012 *Phys. Rev. Lett.* **109** 166801
[29] Lu H, Long R, and Fang W H 2023 *J. Am. Chem. Soc.* **145** 25887
[30] Siu Z B, Tan S G, and Jalil M B A 2016 *AIP Adv.* **6** 055706
[31] Repin E V and Burmistrov I S 2015 *J. Exp. Theor. Phys.* **121** 509
[32] Pan Z H, Vescovo E, Fedorov A V *et al.* 2011 *Phys. Rev. Lett.* **106** 257004
[33] Wang Y H, Hsieh D, Pilon D *et al.* 2011 *Phys. Rev. Lett.* **107** 207602
[34] Koopmans T 1933 *Physica* **1** 104
[35] Sobota J A, He Y, and Shen Z X 2021 *Rev. Mod. Phys.* **93** 025006
[36] Valla T, Fedorov A V, Johnson P D, and Hulbert S L 1999 *Phys. Rev. Lett.* **83** 2085
[37] Chen C Y, Xie Z J, Feng Y *et al.* 2013 *Sci. Rep.* **3** 2411
[38] Frantzeskakis E, Ramankutty S V, de Jong N *et al.* 2017 *Phys. Rev. X* **7** 041041
[39] Inglesfield J E 1982 *Phys. Bull.* **33** 101
[40] Monserrat B and Vanderbilt D 2016 *Phys. Rev. Lett.* **117** 226801
[41] Zhang H Y, Pincelli T, Jozwiak C *et al.* 2022 *Nat. Rev. Methods Primers* **2** 54
[42] Roushan P, Seo J, Parker C V *et al.* 2009 *Nature* **460** 1106
[43] Wilson R B and Coh S 2020 *Commun. Phys.* **3** 179
[44] Das Sarma S and Wu F 2020 *Ann. Phys.* **417** 168193
[45] Kabanov V V and Alexandrov A S 2008 *Phys. Rev. B* **78** 174514
[46] Valla T, Fedorov A V, Johnson P D *et al.* 1999 *Phys. Rev. Lett.* **83** 2085
[47] Sánchez-Barriga J, Varykhalov A, Braun J *et al.* 2014 *Phys. Rev. X* **4** 011046